

PAPER

Localized surface plasmon resonance-enhanced solar-blind $\text{Al}_{0.4}\text{Ga}_{0.6}\text{N}$ MSM photodetectors exhibiting high-temperature robustness

To cite this article: Shuchi Kaushik *et al* 2022 *Nanotechnology* **33** 145202

View the [article online](#) for updates and enhancements.

You may also like

- [All AlGaIn epitaxial structure solar-blind avalanche photodiodes with high efficiency and high gain](#)
Hualong Wu, Weicong Wu, Hongxian Zhang *et al.*
- [High-performance AlGaIn-based solar-blind avalanche photodiodes with dual-periodic III-nitride distributed Bragg reflectors](#)
Chujun Yao, Xuanchao Ye, Rui Sun *et al.*
- [Magnetic behavior of \$\text{Eu}_3\text{Ni}_4\text{Ga}_4\$: antiferromagnetic order and large magnetoresistance](#)
Anupam, C Geibel and Z Hossain







IOP | ebooks™

Bringing together innovative digital publishing with leading authors from the global scientific community.

Start exploring the collection—download the first chapter of every title for free.

Localized surface plasmon resonance-enhanced solar-blind $\text{Al}_{0.4}\text{Ga}_{0.6}\text{N}$ MSM photodetectors exhibiting high-temperature robustness

Shuchi Kaushik¹ , Subhajit Karmakar¹, Prashant Bisht¹, Che-Hao Liao², Xiaohang Li² , Ravendra Kumar Varshney¹, Bodh Raj Mehta¹  and Rajendra Singh^{1,3} 

¹ Department of Physics, Indian Institute of Technology Delhi, Hauz Khas, New Delhi 110016, India

² Advanced Semiconductor Laboratory, King Abdullah University of Science and Technology (KAUST), Thuwal 23955-6900, Saudi Arabia

³ Nanoscale Research Facility, Indian Institute of Technology Delhi, Hauz Khas, New Delhi 110016, India

E-mail: rsingh@physics.iitd.ac.in

Received 31 October 2021, revised 22 November 2021

Accepted for publication 13 December 2021

Published 12 January 2022



Abstract

The appealing properties of tunable direct wide bandgap, high-temperature robustness and chemical hardness, make $\text{Al}_x\text{Ga}_{1-x}\text{N}$ a promising candidate for fabricating robust solar-blind photodetectors (PDs). In this work, we have utilized the optical phenomenon of localized surface plasmon resonance (LSPR) in metal nanoparticles (NPs) to significantly enhance the performance of solar-blind $\text{Al}_{0.4}\text{Ga}_{0.6}\text{N}$ metal–semiconductor–metal PDs that exhibit high-temperature robustness. We demonstrate that the presence of palladium (Pd) NPs leads to a remarkable enhancement by nearly 600, 300, and 462%, respectively, in the photo-to-dark current ratio (PDCR), responsivity, and specific detectivity of the $\text{Al}_{0.4}\text{Ga}_{0.6}\text{N}$ PD at the wavelength of 280 nm. Using the optical power density of only $32 \mu\text{W cm}^{-2}$ at -10 V , maximum values of $\sim 3 \times 10^3$, 2.7 AW^{-1} , and 2.4×10^{13} Jones are found for the PDCR, responsivity and specific detectivity, respectively. The experimental observations are supported by finite difference time domain simulations, which clearly indicate the presence of LSPR in Pd NPs decorated on the surface of $\text{Al}_{0.4}\text{Ga}_{0.6}\text{N}$. The mechanism behind the enhancement is investigated in detail, and is ascribed to the LSPR induced effects, namely, improved optical absorption, enhanced local electric field and LSPR sensitization effect. Moreover, the PD exhibits a stable operation up to 400 K, thereby exhibiting the high-temperature robustness desirable for commercial applications.

Supplementary material for this article is available [online](#)

Keywords: AlGa_xN, solar-blind photodetector, localized surface plasmon resonance, responsivity, specific detectivity, high-temperature robustness

(Some figures may appear in colour only in the online journal)

Introduction

The ultra-violet (UV) photodetectors (PDs) have an ever-increasing demand in the fields of healthcare, space science

and technology, and defense. A few applications requiring UV PDs are environmental monitoring, sanitization, chemical analysis, UV dosimetry, UV astronomy, UV imaging, secure communication, and early missile warning systems [1–3]. To

avoid the chances of false detection, it is essential to sense the UV radiation without detecting the dominant visible or infrared background from the Sun. A solar-blind PD is the one that does not 'see' the Sun, and therefore, responds only to the UV radiations that are shorter than the solar radiation reaching the Earth's surface after atmospheric absorption. By definition, a solar-blind PD is insensitive to photons with wavelengths longer than 285 nm [4]. The common wide bandgap semiconductors such as GaN, SiC, and ZnO have been investigated for successful visible-blind photodetection [5–7]. However, the solar-blind operation requires the focus on ultra-wide bandgap materials [8–10]. Owing to its appealing properties of tunable direct wide bandgap (3.4–6.2 eV), high-temperature robustness, chemical, and radiation hardness, $\text{Al}_x\text{Ga}_{1-x}\text{N}$ has emerged as the most suitable candidate for fabricating the commercial solar-blind PDs [11–14]. Nevertheless, the performance of a market-ready PD is evaluated in terms of the '5 S' requirements of high spectral selectivity, sensitivity, speed, signal-to-noise ratio, and stability [15]. Therefore, there is a need to explore novel strategies to improve these figures of merit for the $\text{Al}_x\text{Ga}_{1-x}\text{N}$ -based solar-blind PDs so that they find the deserving place in the commercial applications.

In the last two decades, the interaction between the plasmonic NPs and semiconductors has proved to be a promising strategy to enhance the performance of semiconductor PDs. The term 'plasmonic' mainly refers to the localized surface plasmon resonance (LSPR) and its induced effects [16]. Driven by the electric field of the external electromagnetic radiation, the free electrons of metal NPs are periodically displaced with respect to the lattice ions. The displacement leads to charges at the opposite surfaces, which tend to attract each other. Therefore, there also exists a restoring force that results in an electron oscillator. The quantum of these oscillations is called a surface plasmon (SP), whose frequency is determined by the composition, shape and size of the metal NPs, and the surrounding dielectric medium. When the oscillation frequency matches with the frequency of the external optical field, surface plasmon resonance (SPR) occurs. In metal NPs, the resonant excitation of the SPs is localized around the NP and consequently termed as LSPR [17–20]. LSPR has been utilized to improve the performance of semiconductor UV PDs. Li *et al* demonstrated that nanoplasmonic enhancement could be applied to the UV region by using Ag NPs for enhancing the performance of GaN PDs [21]. Butun *et al* obtained plasmonic enhancement in the GaN UV PDs by Al NPs [22]. Later, Au NPs were also used to improve visible-blind UV PDs fabricated on GaN [23] and SiC [6]. The impact of different NPs on Ga_2O_3 solar-blind PDs has been studied by a few research groups who utilized Ag [24], Ga [25], Pt [26], and Rh [27] NPs for this purpose.

Unlike Ga_2O_3 , there are very few reports on LSPR mediated performance of $\text{Al}_x\text{Ga}_{1-x}\text{N}$ solar-blind PDs. Bao *et al* studied the enhanced performance of $\text{Al}_{0.4}\text{Ga}_{0.6}\text{N}$ solar-blind PD with Al NPs. However, the reported responsivity was only 0.288 AW^{-1} at 5 V [28]. Zhang *et al* also reported LSPR mediated enhancement in $\text{Al}_{0.4}\text{Ga}_{0.6}\text{N}$ solar-blind PD by Al NPs. The peak responsivity could reach just

2.34 AW^{-1} at a high voltage of 20 V [29]. In addition, other important performance parameters such as specific detectivity, multi-cycle response, and high-temperature stability of the PDs were not investigated in these reports. In comparison to conventional metal NPs (such as Ag and Au), Al exhibits high bulk plasma frequency. As a result, its LSPR occurs in the UV region, and it can be a perfect choice for deep UV PDs [30]. However, the low melting point of Al ($\sim 660^\circ\text{C}$) [31] restricts its usage in the fields requiring robust solar-blind PDs that can withstand high temperatures. Therefore, there is a need to explore metal NPs with high chemical and thermal stability that may prove to be better than Al NPs for improving the performance of $\text{Al}_x\text{Ga}_{1-x}\text{N}$ solar-blind PDs. In recent years, Palladium (Pd) has emerged as a promising plasmonic material for UV applications due to its high bulk plasma frequency. Pd NPs have been explored for photocatalysis, Raman spectroscopy, and DNA biosensing in the UV region [32–34]. Moreover, Pd exhibits superior thermal stability than Al due to its high melting point ($\sim 1552^\circ\text{C}$) [35]. These appealing properties make Pd NPs an ideal choice for enhancing the performance of robust $\text{Al}_x\text{Ga}_{1-x}\text{N}$ solar-blind PDs. Though Pd exhibits extraordinary properties, less effort has been made to investigate its role in solar-blind PDs. Recently, palladium (Pd) NPs have been utilized for LSPR enhanced diamond PDs [32, 36].

In this work, we have investigated the role of Pd NPs in improving the performance of $\text{Al}_{0.4}\text{Ga}_{0.6}\text{N}$ solar-blind PD. Besides studying the impact on various performance parameters such as PDCR, responsivity, and specific detectivity, we have also reported the multi-cycle response of the LSPR mediated PD. In addition, the experimental observations have been supported by finite difference time domain (FDTD) simulations, and the mechanism behind the enhancement has been analysed in detail. Further, to examine the usefulness of the PD for practical applications, we have studied the dependence of various performance parameters on the incident power density. Moreover, the robustness of the PD has been established by exploring the photodetection parameters up to a high-temperature of 400 K.

Methods

The $\text{Al}_{0.4}\text{Ga}_{0.6}\text{N}$ epitaxial film (500 nm thick) used in this study was grown over the AlN template on sapphire by metal organic chemical vapor deposition (MOCVD, Taiyo Nippon Sanso, SR4000 HT). The 2 inch wafer was diced into small pieces of dimensions $5 \text{ mm} \times 5 \text{ mm}$. The pristine samples were cleaned by ultrasonication for 5 min each in de-ionized (DI) water, acetone, and isopropyl alcohol (IPA). After that, the cleaned samples were dried using a dry nitrogen jet. The schematic representation of the samples used in this study, the x-ray diffraction (XRD) 2Theta-omega curve, the Tauc's plot, and the corresponding atomic force microscope scan are given in figure S1 (available online at stacks.iop.org/NANO/33/145202/mmedia) of the supplementary information. Some of the samples were utilized for device fabrication and characterization, while others were for sample characterizations.

For device fabrication, the interdigitated electrode (IDE) geometry of the MSM PD was fabricated using mask-less optical lithography (Intelligent Micropatterning SF-100 Xpress) and Pt/Au (30 nm/60 nm) contacts were deposited by sputtering. Lift-off was performed in warm acetone to obtain the $\text{Al}_{0.4}\text{Ga}_{0.6}\text{N}$ MSM PDs with electrode width and inter-electrode spacing of 20 μm each. The Pd NPs were deposited using an integrated gas-phase synthesis system on the $\text{Al}_{0.4}\text{Ga}_{0.6}\text{N}$ epitaxial films as well as on some of the $\text{Al}_{0.4}\text{Ga}_{0.6}\text{N}$ MSM PDs. It consists of an aerosol generator (GFG 1000 manufactured by PALAS GmbH) for forming Pd nano agglomerates, a sintering furnace for converting the agglomerates into compact spherical particles during an in-flight sintering process, and an electrostatic precipitator to deposit NPs onto the desired substrates as illustrated by the schematic in figure S2 of the supplementary information. After deposition, the samples were annealed at 500 $^{\circ}\text{C}$ in the argon gas environment for 1 h. Since annealing at higher temperatures can affect the contact resistance of metal electrode with the $\text{Al}_{0.4}\text{Ga}_{0.6}\text{N}$ epitaxial film, the $\text{Al}_{0.4}\text{Ga}_{0.6}\text{N}$ PDs without (w/o) NPs were also annealed under the same conditions. This ensured that the change in the contact resistance was equal for both the PDs, with and w/o NPs. The samples decorated with NPs were characterized by field-emission scanning electron microscopy (FESEM, JSM-7800F Prime) and UV-vis spectroscopy (Hitachi, U-3900H Spectrophotometer). The current-voltage (I - V) and current-time (I - t) characteristics of the $\text{Al}_{0.4}\text{Ga}_{0.6}\text{N}$ MSM PDs with and w/o Pd NPs were performed by Keithley semiconductor characterization system (SCS-4200) connected to the EverBeing DC probe station (EB-6). For performing the measurements under illumination, a xenon lamp (75 W) connected to a monochromator (Bentham TMC 300) was employed. The wavelength of interest was incident on the device using a UV-compatible optical fiber (PCU-1000). The power of the incident light was measured by a power meter (Thor laboratories, PM-100D) connected to a calibrated Si detector (Thor laboratories, S130VC). A temperature controller (EverBeing) connected to the DC probe station was used to test the photodetectors with varying temperatures. Further, the absorbance spectrum of the Pd NPs and electric field intensity distribution were explored by performing theoretical simulation of periodically arranged NPs in commercially available CST microwave studio software by FDTD method using periodic boundary conditions.

Results and discussion

Characterization of Pd NPs

To explore the role played by Pd NPs in the photodetection properties of $\text{Al}_{0.4}\text{Ga}_{0.6}\text{N}$ solar-blind PD, it was essential to study the particle distribution and the absorption spectra of the NPs.

The distribution of the NPs was analysed by FESEM, and the absorption spectrum was recorded from the UV-vis spectrophotometer. Figure 1(a) shows the FESEM image of the Pd NPs on the $\text{Al}_{0.4}\text{Ga}_{0.6}\text{N}$ epitaxial film. It can be seen that the size as well as the inter-particle separation are distributed in a wide range. The mean diameter and inter-particle

distance were calculated to be ~ 20 and ~ 60 nm, respectively. Further, the absorbance spectrum of the NPs was recorded and is shown in figure 1(b). As the wavelength was reduced from 500 to 200 nm, the absorbance was found to increase, reaching a value of 0.6 at 200 nm. This shows that the presence of Pd NPs on $\text{Al}_{0.4}\text{Ga}_{0.6}\text{N}$ facilitates the absorption of the incident light, which may enhance the generation of electron-hole pairs in $\text{Al}_{0.4}\text{Ga}_{0.6}\text{N}$ based PD. To confirm this hypothesis, the absorbance spectrum of the Pd NPs was also simulated by the FDTD method for different particle sizes. The simulation results agree with the experimentally recorded spectrum (figure S3 of the supplementary information) and indicate an enhanced absorption due to the Pd NPs.

Impact of Pd NPs on the illumination current of $\text{Al}_{0.4}\text{Ga}_{0.6}\text{N}$ MSM PD

To investigate the impact of Pd NPs on the performance of $\text{Al}_{0.4}\text{Ga}_{0.6}\text{N}$ solar-blind PD, the I - V and I - t characteristics of the PDs with and w/o Pd NPs were studied in the presence of light (as represented in figure 2(a)). The wavelength of the incident light was varied in a broad range from 220 nm (deep UV) to 500 nm (visible). Figure 2(b) shows the I - V characteristics of both the PDs in the dark and under the illumination of 500 and 280 nm (corresponding to the bandgap of $\text{Al}_{0.4}\text{Ga}_{0.6}\text{N}$). For the PD fabricated on the pristine $\text{Al}_{0.4}\text{Ga}_{0.6}\text{N}$ film, i.e. w/o NPs, the current at 500 nm was found to be almost the same as that of the dark current. In comparison, the current at 280 nm (solar-blind region) was observed to be ~ 3 orders higher than the dark current. On decorating the $\text{Al}_{0.4}\text{Ga}_{0.6}\text{N}$ film by Pd NPs, a clear enhancement in the current at 500 and 280 nm was observed. At 10 V, for the PD w/o NPs, the current was found to be 3.5×10^{-11} A and 2.4×10^{-8} A at 500 and 280 nm, respectively. On the other hand, for the PD with NPs, the higher current values of 8.3×10^{-10} A and 1.0×10^{-7} A were recorded at 500 and 280 nm, respectively. Also, we found that the dark current increased slightly for the PD decorated with Pd NPs. For example, at 10 V, the dark current w/o NPs was found to be 3.5×10^{-11} A, and it increased to 8.7×10^{-11} A for the PD decorated with Pd NPs. This is attributed to the presence of defect states at the interface between Pd NPs and $\text{Al}_{0.4}\text{Ga}_{0.6}\text{N}$, which act as traps and result in higher dark current in the PD decorated with the NPs [16].

To have a clear idea of the enhancement in the current values by Pd NPs, we calculated the PDCR of the PDs, which is given by [1, 37]

$$PDCR = \frac{I_{\lambda} - I_d}{I_d}, \quad (1)$$

where, I_{λ} is the illumination current at the incident wavelength of λ (also known as 'on-current'), and I_d is the dark current (also known as 'off-current'). The plot of PDCR of the PDs with and w/o NPs at 500 and 280 nm is shown in figure 2(c). The average percentage increase was found to be more than 3×10^4 and 6×10^2 % at 500 and 280 nm, respectively. Next, to examine the response of the PDs to the repeatedly switching input optical signal, I - t characteristics were performed at -5

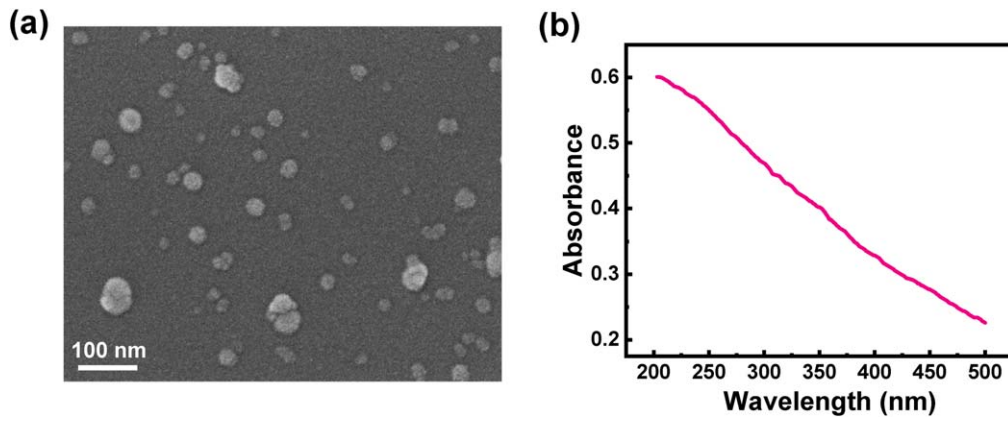


Figure 1. (a) FESEM image of the Pd NPs on Al_{0.4}Ga_{0.6}N epitaxial film. (b) The experimentally observed absorbance spectrum of the NPs.

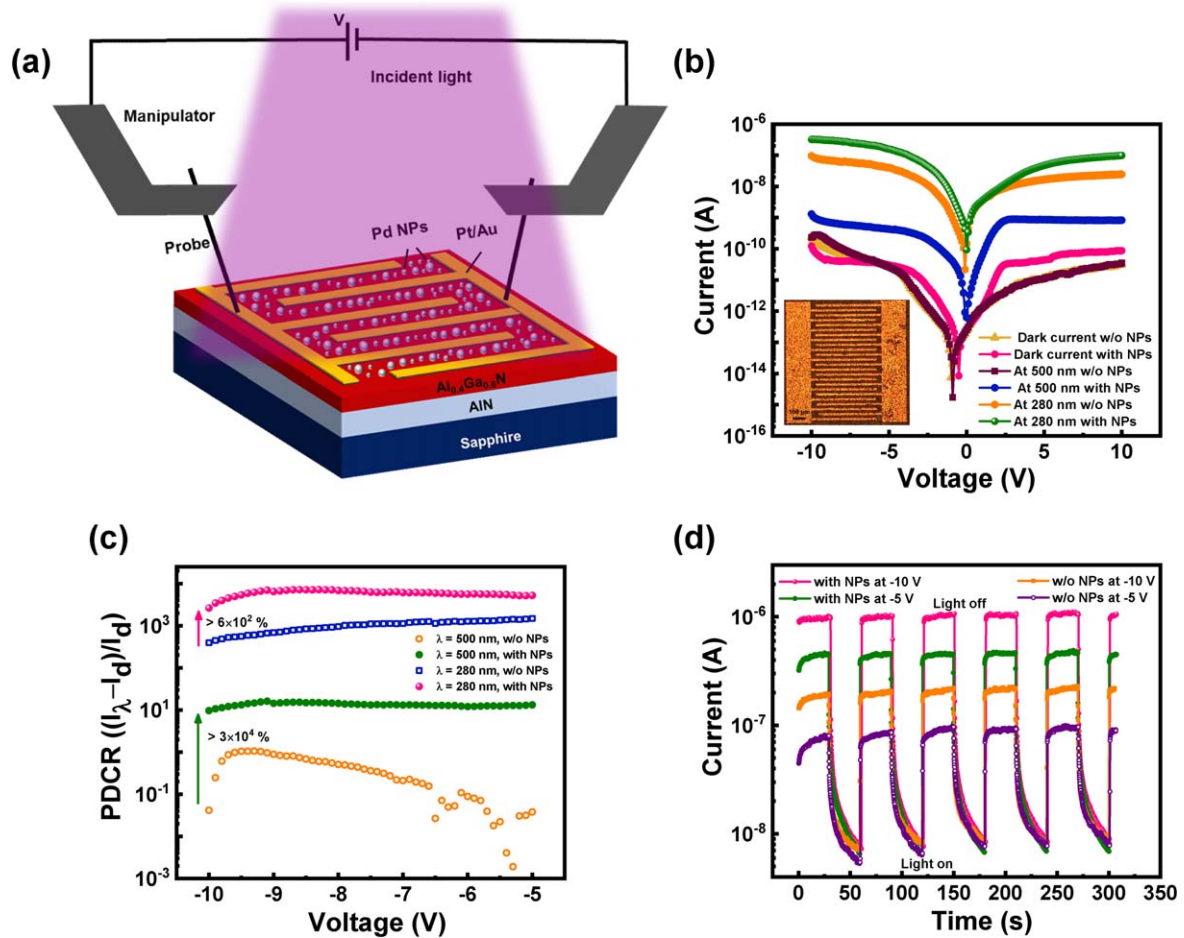


Figure 2. (a) Schematic illustration of the electrical characterization of as-fabricated Al_{0.4}Ga_{0.6}N MSM PD decorated with Pd NPs in the presence of light. (b) I - V characteristics of Al_{0.4}Ga_{0.6}N PD with and w/o Pd NPs in the dark and in the presence of the light of wavelength 500 and 280 nm. The inset shows the optical microscope image of the fabricated device. (c) The plot of PDCR with voltage for the incident wavelength of 500 and 280 nm for the Al_{0.4}Ga_{0.6}N PDs with and w/o Pd NPs. (d) I - t characteristics of the two PDs following the repeated on and off cycles of the incident light of 280 nm at -5 and -10 V.

and -10 V at a fixed wavelength of 280 nm. Figure 2(d) shows the multi-cycle response of the PDs. It was observed that the current was found to rise (fall) on switching on (off) the light

signal periodically. Moreover, the curves clearly represent an enhancement in the on-current (current on switching on the light) for the Al_{0.4}Ga_{0.6}N PD with Pd NPs.

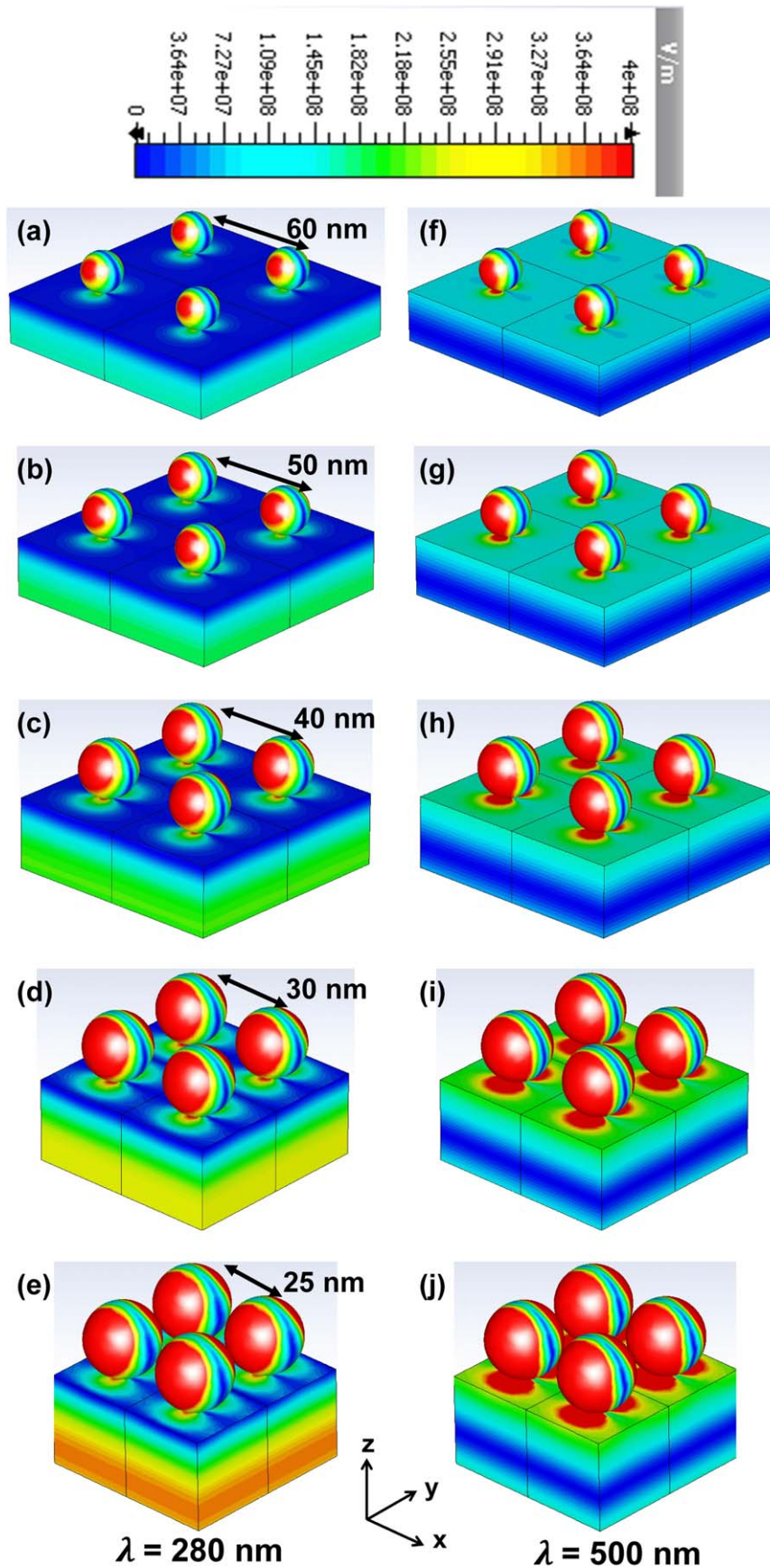


Figure 3. The 3D representation of electric field intensity distribution corresponding to the incident wavelength of (a)–(e) 280 nm and (f)–(j) 500 nm in Pd NPs decorated on the surface of $\text{Al}_{0.4}\text{Ga}_{0.6}\text{N}$. The size of the NPs in each figure is 20 nm, whereas the inter-particle separation has been taken as: 60 (a), (f), 50 (b), (g), 40 (c), (h), 30 (d), (i), and 25 (e), (j) nm.

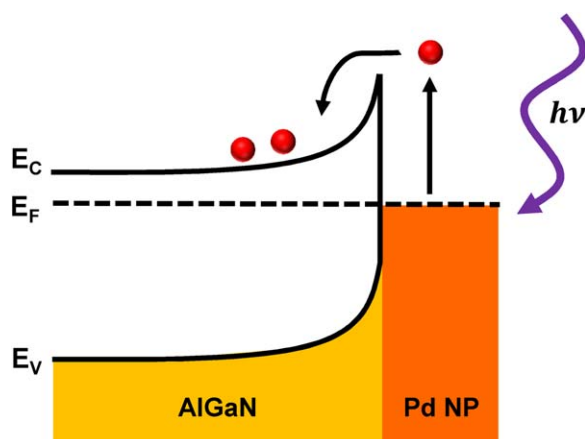


Figure 4. The energy band diagram showing the LSPR sensitization effect resulting in an increase in the number of conduction band electrons in $\text{Al}_{0.4}\text{Ga}_{0.6}\text{N}$. The diagram depicts the excitation of free electrons of Pd NP to high energy state upon interaction with the incident light, leading to the direct transfer of electrons over the Schottky barrier to the conduction band of $\text{Al}_{0.4}\text{Ga}_{0.6}\text{N}$.

Investigation of the mechanism behind the enhanced on-current

On performing I - V and I - t characterization of the as-fabricated PDs, it was clear that the NPs led to significant enhancement in the on-current and hence PDCR of the device. Moreover, the percentage change at 500 nm was greater than at 280 nm. The mechanism behind the observed results was explored by performing theoretical simulation of periodically arranged NPs by FDTD method using periodic boundary conditions. Here, adaptive tetrahedral meshing was adapted to calculate the effective absorbance spectra and electromagnetic field confinement at desired wavelengths. Figure 1(a) illustrates that the Pd NPs vary in size and separation with average particle size and separation of ~ 20 and ~ 60 nm, respectively. Therefore, to find the correlation with the experimental results, we investigated the electric field intensity distribution for the periodic arrangement of spherical particles of size 20 nm by varying the inter-particle distance from 25 to 60 nm. Figure 3 illustrates the 3D electric field intensity distribution for different arrangements of Pd NPs on $\text{Al}_{0.4}\text{Ga}_{0.6}\text{N}$ for the linearly polarized (along x or y) incident light of wavelengths 500 and 280 nm. The simulated results demonstrate the 3D representation of the electric field intensity distribution in Pd NPs, which clearly indicates the presence of LSPR in the NPs at both wavelengths. The LSPR in NPs results in an enhanced local electric field in $\text{Al}_{0.4}\text{Ga}_{0.6}\text{N}$, which is also evident from the figure. It has been reported that the rate of electron-hole pair generation in a semiconductor is proportional to the local electric field intensity [16]. Therefore, in addition to the improved absorbance due to Pd NPs (figure S3), the LSPR enhanced local electric field facilitates the generation of more charge carriers in $\text{Al}_{0.4}\text{Ga}_{0.6}\text{N}$, and effectively favours the separation of electron-hole pairs, which increase the on-current of the photodetector significantly. Next, comparing the electric field intensity distributions at 500 and 280 nm, it is clear that the

LSPR induced local field enhancement is more at 500 nm than at 280 nm. This explains the higher percentage change in the PDCR (figure 2(c)) at 500 nm. Furthermore, since 280 nm corresponds to the bandgap of $\text{Al}_{0.4}\text{Ga}_{0.6}\text{N}$, the field intensity in bulk $\text{Al}_{0.4}\text{Ga}_{0.6}\text{N}$ is higher at 280 nm than 500 nm. As a result, the net magnitude of the illumination current at 280 nm is more than the current at 500 nm, even in the presence of the NPs. Moreover, the electric field intensity enhances on decreasing the particle separation from 60 to 25 nm, which is due to the increased inter-unit cell coupling of plasmonic nanoparticles and correspondingly larger generation of LSPR. Additionally, it follows the same trend for different inter-particle distances for the incident wavelength of 500 and 280 nm.

From the above discussion, we can deduce that the LSPR induced enhanced optical absorption and local electric field led to an enhancement in the on-current at 500 and 280 nm wavelengths. It is interesting to note that the presence of NPs led to the illumination current at sub-bandgap excitation of 500 nm, which otherwise is not possible in the PD w/o NPs. Therefore, we can infer that due to NPs, there is no need to excite the electrons from valence to the conduction band of $\text{Al}_{0.4}\text{Ga}_{0.6}\text{N}$ to enhance the current upon illumination. In fact, due to the high work function of Pd, a Schottky barrier exists between Pd NPs and $\text{Al}_{0.4}\text{Ga}_{0.6}\text{N}$, which allows sub-bandgap photocurrents due to the LSPR sensitization effect [16, 38]. The energy of LSPR is dissipated by two competitive pathways, namely radiative and non-radiative decay. The former involves the release of energy by the emission of a photon. However, this process is less dominant than non-radiative decay, which serves as the primary contributor in the SPR decay. One of the non-radiative processes is the LSPR sensitization effect, a dominant electron-electron relaxation mechanism that governs the decay of LSPR and explains the observed results in our experiment [16]. Figure 4 illustrates the mechanism of the LSPR sensitization effect. As shown in the figure, a Schottky barrier exists between $\text{Al}_{0.4}\text{Ga}_{0.6}\text{N}$ and Pd NP which prevents the flow of free electrons from NP to $\text{Al}_{0.4}\text{Ga}_{0.6}\text{N}$. As a result of resonance with the incident light, a large number of electrons of Pd NP are excited to higher energy levels, even higher than the conduction band edge of $\text{Al}_{0.4}\text{Ga}_{0.6}\text{N}$. This facilitates the direct transfer of electrons to the conduction band of $\text{Al}_{0.4}\text{Ga}_{0.6}\text{N}$, which result in the enhanced illumination current in $\text{Al}_{0.4}\text{Ga}_{0.6}\text{N}$ solar-blind PD decorated with Pd NPs. This process continues till the energy of electrons remains higher than the Schottky barrier height (SBH). After complete dissipation of the LSPR energy through electron-electron collisions, the electrons in the Pd NP return to the equilibrium state [16, 39–42]. For the LSPR sensitization effect, the energy of incident photons should be greater than the SBH formed by Pd NP on $\text{Al}_{0.4}\text{Ga}_{0.6}\text{N}$. As a result, even sub-bandgap excitation (with energy more than the SBH) can lead to this effect. Typically, the SBH of ~ 1 eV has been reported for Pd/AlGaIn Schottky contacts [43–45]. Therefore, the interaction of Pd NPs with the incident wavelengths from 220 to 500 nm can inject the electrons in the conduction band of $\text{Al}_{0.4}\text{Ga}_{0.6}\text{N}$ and enhance the on-current. This explains the enhancement in the on-current at

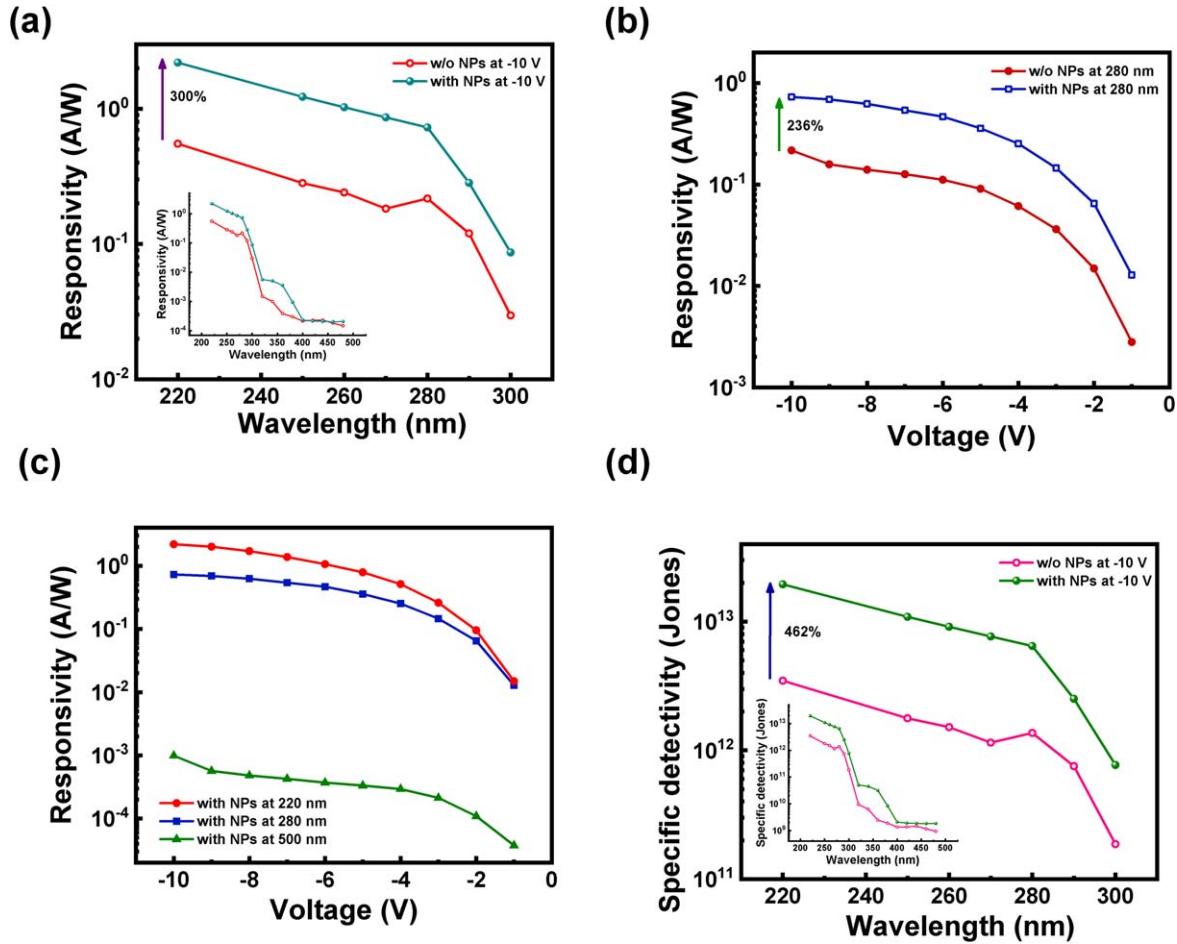


Figure 5. (a) The variation of responsivity at -10 V with incident wavelength (220–300 nm) for the $\text{Al}_{0.4}\text{Ga}_{0.6}\text{N}$ solar-blind PD with and w/o Pd NPs. The inset shows the variation in a broad spectral range from 220 to 500 nm. (b) The variation of responsivity with voltage at 280 nm for both the PDs. (c) The plot of responsivity with voltage at 500, 280, and 220 nm for $\text{Al}_{0.4}\text{Ga}_{0.6}\text{N}$ PD decorated with Pd NPs. (d) The variation of specific detectivity at -10 V with incident wavelength (220–300 nm) for the $\text{Al}_{0.4}\text{Ga}_{0.6}\text{N}$ solar-blind PD with and w/o Pd NPs. The inset shows the variation in a broad spectral range from 220 to 500 nm.

sub-bandgap wavelength of 500 nm. On the other hand, the higher percentage change in the on-current at 500 nm than 280 nm is explained by the LSPR enhanced local electric field, which is more at 500 nm.

Impact of Pd NPs on the performance parameters of $\text{Al}_{0.4}\text{Ga}_{0.6}\text{N}$ MSM PD

As a result of enhancement in the on-current due to Pd NPs, the performance parameters of the as-fabricated PD were found to improve significantly. The responsivity (R_λ) is one of the key parameters to evaluate the PD's performance and is given by [37, 46]

$$R_\lambda = \frac{I_\lambda - I_d}{P_\lambda}, \quad (2)$$

where, P_λ is the incident optical power corresponding to the wavelength λ . Figure 5(a) shows the plot of responsivity of both the PDs with incident wavelength varying from 220 to 300 nm. inset represents the variation in a broader range from 220 to 500 nm. The figure clearly indicates that though the

illumination current was found to increase at 500 nm due to the presence of NPs, no significant change was observed in the responsivity of the PD in the visible region. Moreover, an appreciable value of responsivity was calculated for the solar-blind region (wavelengths shorter than 280 nm) and was found to improve significantly due to the presence of Pd NPs. At -10 V, the peak responsivity was found to increase by 300%, reaching a maximum value of 2.2 A/W at 220 nm with an incident optical power of only $1.7 \mu\text{W}$. This indicates that the fabricated PD is capable of detecting even weak signals. Further, figure 5(b) shows the variation of responsivity at 280 nm with the applied voltage. It was observed that the responsivity increased with the increasing bias. This is ascribed to the increase in electric field with the increasing applied voltage, which facilitates the separation of the charge carriers. At -10 V, an enhancement by 236% was observed in the responsivity at 280 nm for the PD with NPs. Figure 5(c) indicates the plot of responsivity versus voltage for the PD with NPs at three different wavelengths. The figure clearly demonstrates that the as-fabricated $\text{Al}_{0.4}\text{Ga}_{0.6}\text{N}$ PD with Pd

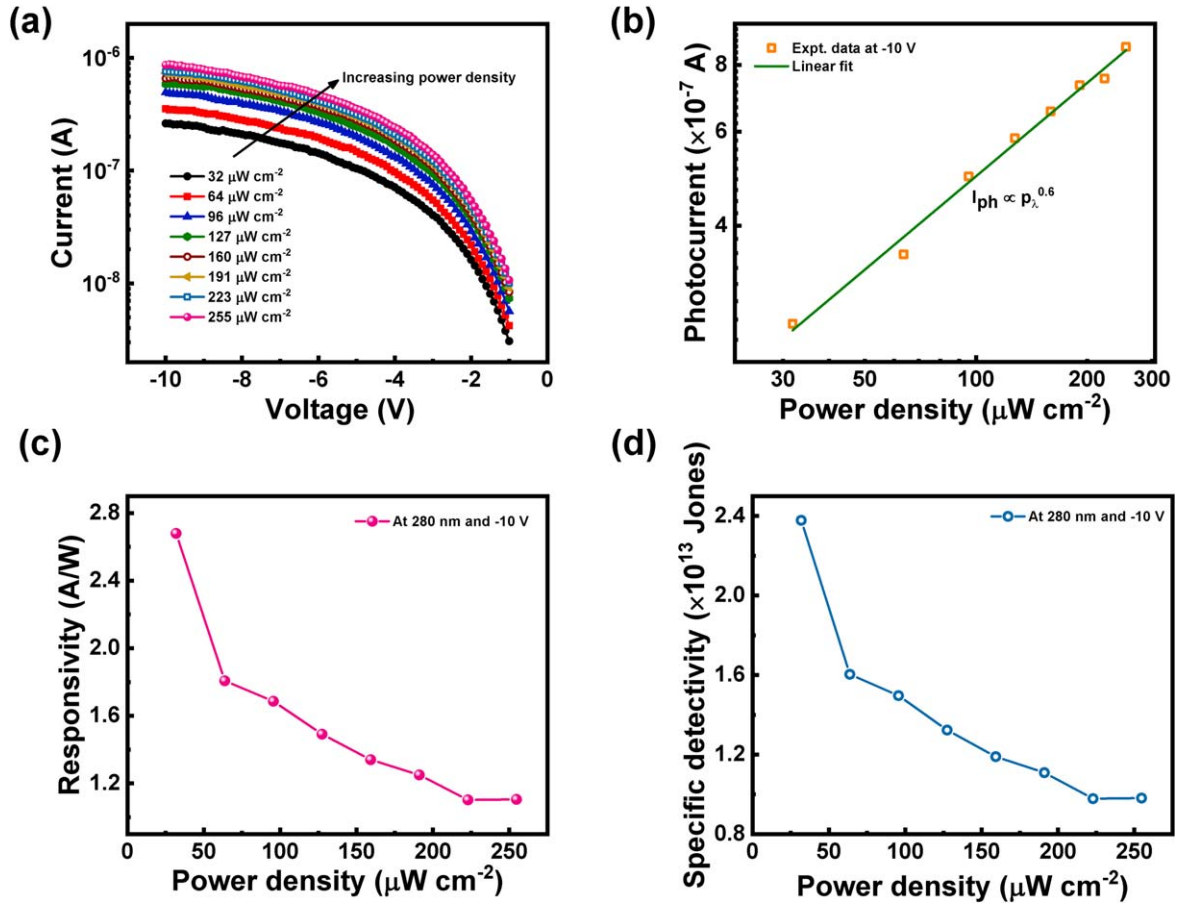


Figure 6. (a) I - V characteristics of LSPR enhanced $\text{Al}_{0.4}\text{Ga}_{0.6}\text{N}$ solar-blind PD with varying incident optical power density under the illumination of 280 nm. (b) The power-law dependence of the photo-current on the incident power density, giving the empirical constant = 0.6. (c) Variation of responsivity and (d) specific detectivity with the incident power density at 280 nm and -10 V.

NPs has a very weak response at the visible wavelength of 500 nm. The device shows high responsivity in the solar-blind region with the peak values of 0.7 AW^{-1} and 2.2 AW^{-1} at 280 and 220 nm, respectively.

To compare the sensitivity of the PDs, we calculated the specific detectivity (D^*), which is given by the following expression [1]

$$D^* = R_\lambda \sqrt{\frac{A}{2eI_d}}, \quad (3)$$

where A is the active device area ($\sim 0.3 \text{ mm}^2$). Figure 5(d) shows the plot of specific detectivity of both the PDs with wavelength varying from 300 to 220 nm and the variation in a broader range is given in the inset. Similar to the responsivity, a significant improvement in the specific detectivity was observed in the solar-blind region. The maximum value was found to increase by 462%, and a peak value of 1.9×10^{13} Jones was calculated at -10 V. It is clear that though illumination current increased in the visible region, the performance parameters such as responsivity and specific detectivity showed a significant enhancement in the solar-blind region for the $\text{Al}_{0.4}\text{Ga}_{0.6}\text{N}$ MSM PD with Pd NPs.

Investigation of the performance parameters with the varying incident optical power density and working temperature

To examine the usefulness of the LSPR enhanced $\text{Al}_{0.4}\text{Ga}_{0.6}\text{N}$ MSM PD, we studied its response by varying the incident optical power density (p_λ) at a fixed wavelength of 280 nm. As shown in figure 6(a), the on-current (I_λ) was found to increase on increasing the optical power density from 32 to 255 $\mu\text{W cm}^{-2}$. This is because on increasing the incident optical power density, the number of photogenerated carriers contributing to I_λ increase. For a PD, the photoresponse obeys the power law, which is given by:

$$I_{ph} = A p_\lambda^c, \quad (4)$$

where, I_{ph} is the photo-current ($I_\lambda - I_d$), A is the proportionality constant, and c is the empirical coefficient [47]. According to equation (4), on fitting the experimental data linearly, the value of c can be found from the slope of the curve. Figure 6(b) shows the linear fit of the photocurrent versus power density, and the slope gave $c = 0.6$. The low value of c (< 1) indicates the presence of trap states due to Pd NPs that may act as recombination centres upon illumination [5, 47]. This observation also verifies the reason stated earlier for a slight increase in the dark current for the PD with NPs.

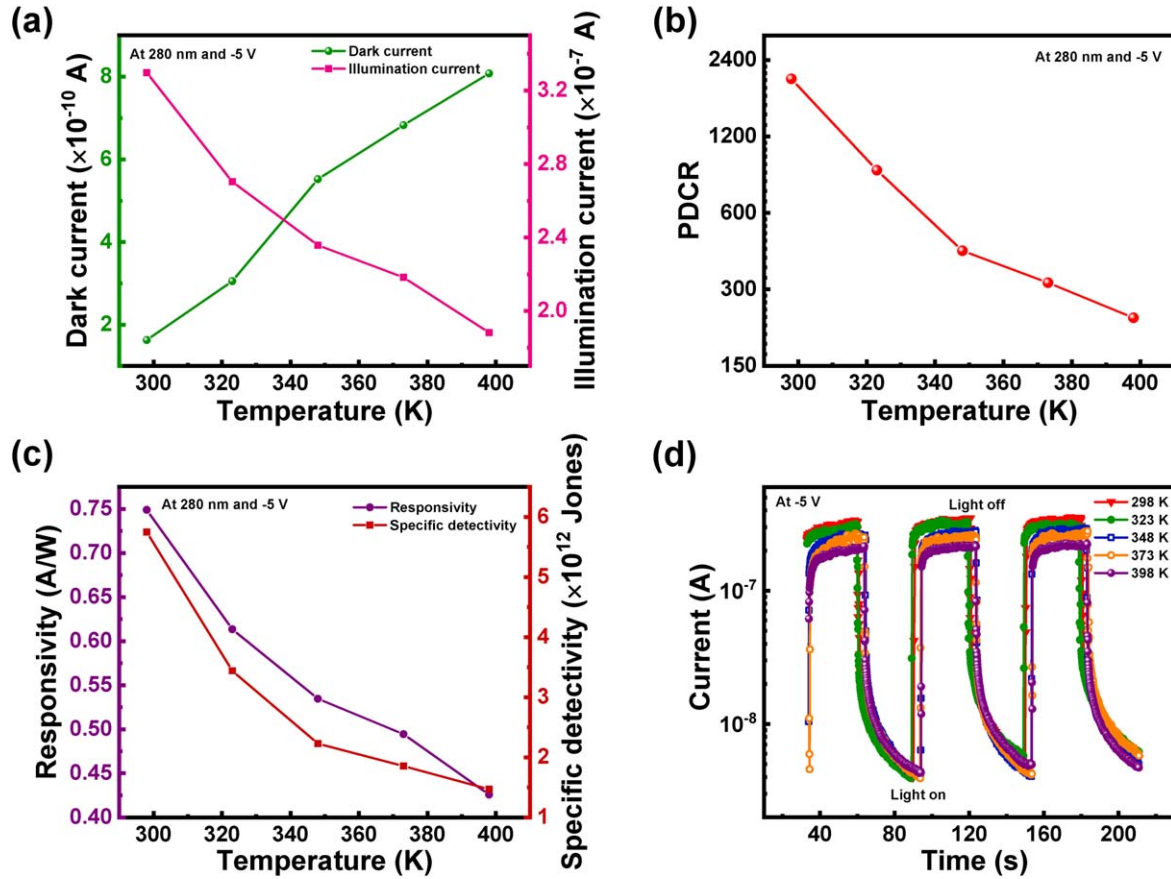


Figure 7. Variation of (a) dark and illumination current, (b) PDCR, (c) responsivity and specific detectivity of LSPR enhanced $\text{Al}_{0.4}\text{Ga}_{0.6}\text{N}$ solar-blind PD with temperature varying from 298 to 398 K. (d) The multi-cycle response showing the stability of the PD up to a high-temperature of 398 K.

Further, we examined the dependence of the responsivity and specific detectivity on the incident optical power density (figures 6(c), (d)). Equations (2) and (4) imply that responsivity should remain constant if the variation of I_{ph} with P_{λ} obeys an exact linear relationship. The value of c being less than 1 suggests that the responsivity and hence specific detectivity (refer to equation (3)) decrease with the increasing incident power density, which is consistent with the observed results. The maximum values of 2.7 A/W^{-1} and $2.4 \times 10^{13} \text{ Jones}$ were calculated for responsivity and specific detectivity, respectively by using an incident optical power density of only $32 \mu\text{W cm}^{-2}$ at the incident wavelength of 280 nm at -10 V .

Further, to examine the practicality of the LSPR enhanced solar-blind PD, we tested the device by varying the working temperature from room temperature (RT) to 400 K. The variation of dark (off), and illumination (on) current with temperature was plotted and is shown in figure 7(a). The dark current was found to increase on increasing the temperature, whereas the illumination current followed the opposite trend. On increasing the temperature, the number of thermally generated carriers increases, which leads to an increase in the dark current [37]. On the other hand, the recombination process of the photogenerated carriers increases significantly on increasing the temperature and leads to a decrease in the illumination current [48, 49]. The performance of a PD can be better evaluated by studying PDCR with temperature.

Figure 7(b) shows that the PDCR reduced from 2024 to 232 at -5 V on increasing the temperature from 298 to 398 K. Therefore, even at a high working temperature, the device exhibited solar-blind operation with a high PDCR of 232. Further, the variation of responsivity and specific detectivity with temperature is given in figure 7(c). At -5 V , the responsivity reduced from 0.75 to 0.43 A/W^{-1} , and specific detectivity decreased from 5.7×10^{12} to $1.4 \times 10^{12} \text{ Jones}$ on increasing the temperature from RT to 398 K. Next; we examined the multi-cycle response of the PD at high temperatures. As can be seen from figure 7(d), even on increasing the temperature to 398 K, the PD could efficiently respond to the switching input signal. These observations established that the PD could detect the incident solar-blind wavelengths even at a high temperature of $\sim 400 \text{ K}$. Therefore, we can deduce that the LSPR enhanced $\text{Al}_{0.4}\text{Ga}_{0.6}\text{N}$ solar-blind exhibited high-temperature robustness with high PDCR, responsivity, and specific detectivity.

A comparison of different PDs where NPs have been utilized to improve the performance parameters is given in table 1. The table shows that the $\text{Al}_{0.4}\text{Ga}_{0.6}\text{N}$ PD fabricated in this work by using Pd NPs exhibits significantly high values of responsivity and specific detectivity at low bias voltage in the solar-blind region by using ultra-low incident optical power density. In addition, the LSPR mediated PD studied in

Table 1. A comparison of various reports utilizing NPs for the performance enhancement of visible-blind and solar-blind PDs.

Type of the PD	Active layer	Metal NP	Wavelength (nm)	Power density ($\mu\text{W cm}^{-2}$)	Voltage (V)	Responsivity (AW^{-1})	Specific detectivity (Jones)	High-temperature robustness	References
Visible-blind	GaN	Ag	360	—	5	4	—	—	[21]
Visible-blind	GaN	Al	340	—	−10	—	—	—	[22]
Visible-blind	GaN	Au	325	—	−3	0.38	3.38×10^{10}	—	[23]
Solar-blind	SiC	Au	254	1.35×10^3	20	—	—	—	[6]
Solar-blind	Ga ₂ O ₃	Ga	254	—	15	2.85	—	—	[25]
Solar-blind	Ga ₂ O ₃	Pt	254	—	−15	29.08	2.16×10^{11}	—	[26]
Solar-blind	Ga ₂ O ₃	Rh	255	—	5	2.76	1.64×10^{13}	—	[27]
Solar-blind	Diamond	Pd	225	10.7	30	9.1	—	—	[36]
Solar-blind	Diamond	Pd	210	—	5	0.057	—	—	[32]
Solar-blind	Al _{0.54} Ga _{0.46} N	Al	270	—	20	2.34	—	—	[29]
Solar-blind	Al _{0.4} Ga _{0.6} N	Al	288	—	5	0.288	—	—	[28]
Solar-blind	Al _{0.4} Ga _{0.6} N	Pd	280	32	−10	2.7	2.4×10^{13}	Yes	This work

this work exhibits high-temperature robustness which is desirable for practical applications.

Conclusions

In conclusion, we have demonstrated the enhanced performance of $\text{Al}_{0.4}\text{Ga}_{0.6}\text{N}$ solar-blind PD by decorating the surface with Pd NPs. An enhancement of more than 600% was observed in the peak PDCR value at the bandgap wavelength of 280 nm. Though the illumination current increased at the visible wavelengths, the performance parameters such as responsivity and specific detectivity showed significant change only in the solar-blind region. The peak responsivity and specific detectivity of the PD were enhanced by 300 and 462%, respectively, at 220 nm. Further, the maximum values of 2.7 AW^{-1} and 2.4×10^{13} Jones were calculated for responsivity and specific detectivity, respectively, by using an incident optical power density of only $32 \mu\text{W cm}^{-2}$ at the incident wavelength of 280 nm at -10 V . The mechanism behind the enhancement was investigated in detail and was ascribed to the LSPR induced effects, viz improved optical absorption, enhanced local electric field and LSPR sensitization effect. Further, we studied the photoresponse with temperature and established the high-temperature robustness of the PD up to 400 K. Since Pd NPs can withstand high temperatures, we believe our study opens up the way towards high-performance plasmonic-enhanced robust AlGaIn solar-blind PDs that can find a place in commercial applications.





Acknowledgments

Shuchi Kaushik acknowledges the Ministry of Education, India for providing the fellowship. The fabrication and characterization facilities provided by Nanoscale Research Facility (NRF) and Central Research Facility (CRF), IIT Delhi are greatly acknowledged.

Data availability statement

All data that support the findings of this study are included within the article (and any supplementary files).

ORCID iDs

Shuchi Kaushik  <https://orcid.org/0000-0002-1927-7945>
 Xiaohang Li  <https://orcid.org/0000-0002-4434-365X>
 Bodh Raj Mehta  <https://orcid.org/0000-0002-2888-5897>
 Rajendra Singh  <https://orcid.org/0000-0002-6890-6904>

References

- [1] Kaushik S and Singh R 2021 2D layered materials for ultraviolet photodetection: a review *Adv. Opt. Mater.* **2002214** 1–20
- [2] Zheng W, Jia L and Huang F 2020 Vacuum-ultraviolet photon detections *iScience* **23** 101145
- [3] Vatansever F, Ferraresi C, de Sousa M V P, Yin R, Rineh A, Sharma S K and Hamblin M R 2013 Can biowarfare agents be defeated with light? *Virulence* **4** 37–41
- [4] Razezghi M 2002 Short-wavelength solar-blind detectors—status, prospects, and markets *Proc. IEEE* **90** 1006–14
- [5] Garg M, Tak B R, Rao V R and Singh R 2019 Giant UV photoresponse of gan-based photodetectors by surface modification using phenol-functionalized porphyrin organic molecules *ACS Appl. Mater. Interfaces* **11** 12017–26
- [6] Mousa H, Yildirim M A and Teker K 2019 Performance enhancement of 3C-SiC thin film UV photodetector via gold nanoparticles *Semicond. Sci. Technol.* **34** 95002
- [7] Liu K, Sakurai M, Liao M and Aono M 2010 Giant improvement of the performance of ZnO nanowire photodetectors by Au nanoparticles *J. Phys. Chem. C* **114** 19835–9
- [8] Kaushik S, Naik T R, Alka A, Garg M, Tak B R, Ravikanth M, Rao V R and Singh R 2020 Surface modification of AlN using organic molecular layer for improved deep uv photodetector performance *ACS Appl. Electron. Mater.* **2** 739–46
- [9] Lin C N et al 2018 Diamond-based all-carbon photodetectors for solar-blind imaging *Adv. Opt. Mater.* **6** 1–7
- [10] Chen Y C, Lu Y J, Lin C N, Tian Y Z, Gao C J, Dong L and Shan C X 2018 Self-powered diamond/ β -Ga₂O₃ photodetectors for solar-blind imaging *J. Mater. Chem. C* **6** 5727–32
- [11] Kaushik S, Naik T R, Ravikanth M, Liao C-H, Li X, Rao V R and Singh R 2021 Organic passivation of $\text{Al}_{0.5}\text{Ga}_{0.5}\text{N}$ epilayers using self-assembled monolayer of Zn(II) porphyrin for improved solar-blind photodetector performance *Semicond. Sci. Technol.* **36** 055001
- [12] Monroy E, Calle F, Muñoz E and Omnes F 1999 AlGaIn metal–semiconductor–metal photodiodes *Appl. Phys. Lett.* **74** 3401
- [13] Xie F, Lu H, Chen D, Ji X, Yan F, Zhang R, Zheng Y, Li L and Zhou J 2012 Ultra-low dark current algan-based solar-blind metal–semiconductor–metal photodetectors for high-temperature applications *IEEE Sens. J.* **12** 2086–90
- [14] Li D, Jiang K, Sun X and Guo C 2018 AlGaIn photonics: recent advances in materials and ultraviolet devices *Adv. Opt. Photonics* **10** 43
- [15] Lu Y J, Lin C N and Shan C X 2018 Optoelectronic diamond: growth, properties, and photodetection applications *Adv. Opt. Mater.* **6** 1–16
- [16] Zhang X, Chen Y L, Liu R S and Tsai D P 2013 Plasmonic photocatalysis *Rep. Prog. Phys.* **76** 046401
- [17] Stockman M I 2011 Nanoplasmonics: the physics behind the applications *Phys. Today* **64** 39–44
- [18] Volkov I N, Yermekova Z S, Khabibrakhmanov A I, Kovalskii A M, Corthey S, Tameev A R, Aleksandrov A E, Sorokin P B, Shtansky D V and Matveev A T 2021 Extended UV detection bandwidth: H-BN/Al powder nanocomposites photodetectors sensitive in a middle UV Region due to localized surface plasmon resonance effect *Epl* **133** 28002
- [19] Wu Y, Sun X J, Jia Y P and Li D B 2018 Review of improved spectral response of ultraviolet photodetectors by surface plasmon *Chin. Phys. B* **27** 126101
- [20] Liu L, Zhangyang X, Lv Z, Lu F and Tian J 2021 Enhanced light trapping in GaN thin films with Al nanoparticles for photocathode applications *Mater. Sci. Eng. B* **269** 115158
- [21] Li D, Sun X, Song H, Li Z, Chen Y, Jiang H and Miao G 2012 Realization of a high-performance GaN UV detector by nanoplasmonic enhancement *Adv. Mater.* **24** 845–9
- [22] Butun S, Cinel N A and Ozbay E 2012 LSPR enhanced MSM UV photodetectors *Nanotechnology* **23** 0–5
- [23] Goswami L et al 2020 Au-nanoplasmonics-mediated surface plasmon-enhanced GaN nanostructured UV photodetectors *ACS Omega* **5** 14535–42

- [24] Arora K, Singh D P, Fischer P and Kumar M 2020 Spectrally selective and highly sensitive UV photodetection with UV-A,C band specific polarity switching in silver plasmonic nanoparticle enhanced gallium oxide thin-film *Adv. Opt. Mater.* **8** 1–9
- [25] Cui S, Mei Z, Hou Y, Sun M, Chen Q, Liang H, Zhang Y, Bai X and Du X 2018 Surface plasmon enhanced solar-blind photoresponse of Ga₂O₃ film with Ga nanospheres *Sci. China Phys., Mech. Astron.* **61** 107021
- [26] Yu J et al 2021 Surface modification of β -Ga₂O₃ layer using Pt nanoparticles for improved deep UV photodetector performance *J. Alloys Compd.* **872** 159508
- [27] Tang R et al 2020 Localized surface plasmon enhanced Ga₂O₃ solar blind photodetectors *Opt. Express* **28** 5731
- [28] Bao G, Li D, Sun X, Jiang M, Li Z, Song H, Jiang H, Chen Y, Miao G and Zhang Z 2014 Enhanced spectral response of an AlGaIn-based solar-blind ultraviolet photodetector with Al nanoparticles *Opt. Express* **22** 24286
- [29] Zhang W et al 2015 High-performance AlGaIn metal–semiconductor–metal solar-blind ultraviolet photodetectors by localized surface plasmon enhancement *Appl. Phys. Lett.* **106** 0–5
- [30] Gerard D and Gray S K 2015 Aluminium plasmonics *J. Phys. D: Appl. Phys.* **48** 184001
- [31] Puri P and Yang V 2007 Effect of particle size on melting of aluminum at nano scales *J. Phys. Chem. C* **111** 11776–83
- [32] Chang X et al 2019 Enhanced ultraviolet absorption in diamond surface via localized surface plasmon resonance in palladium nanoparticles *Appl. Surf. Sci.* **464** 455–7
- [33] Li Z and Meng X 2020 Recent development on palladium enhanced photocatalytic activity: a review *J. Alloys Compd.* **830** 154669
- [34] Li H, Sun D E and Liu Z 2015 Ultrasensitive biosensing platform based on the luminescence quenching ability of plasmonic palladium nanoparticles *Chemistry A* **21** 4944–8
- [35] De Marchi S, Núñez-Sánchez S, Bodelón G, Pérez-Juste J and Pastoriza-Santos I 2020 Pd nanoparticles as a plasmonic material: synthesis, optical properties and applications *Nanoscale* **12** 23424–43
- [36] Chang X et al 2020 Pd nanoparticle size effects in localized surface plasmon-enhanced diamond photodetectors *Opt. Mater.* **107** 110031
- [37] Kaushik S, Sorifi S and Singh R 2021 Study of temperature dependent behavior of H-BN nanoflakes based deep UV photodetector *Photon. Nanostruct. Fundam. Appl.* **43** 100887
- [38] Huang J A and Luo L B 2018 Low-dimensional plasmonic photodetectors: recent progress and future opportunities *Adv. Opt. Mater.* **6** 1701282
- [39] Logunov S L, Ahmadi T S, El-Sayed M A, Khoury J T and Whetten R L 1997 Electron dynamics of passivated gold nanocrystals probed by subpicosecond transient absorption spectroscopy *J. Phys. Chem. B* **101** 3713–9
- [40] Knight M W, Sobhani H, Nordlander P and Halas N J 2011 Photodetection with active optical antennas *Science* **332** 702–4
- [41] White T P and Catchpole K R 2012 Plasmon-enhanced internal photoemission for photovoltaics: theoretical efficiency limits *Appl. Phys. Lett.* **101** 073905
- [42] Zhang Q, Thrithamarassery Gangadharan D, Liu Y, Xu Z, Chaker M and Ma D 2017 Recent advancements in plasmon-enhanced visible light-driven water splitting *J. Mater.* **3** 33–50
- [43] Arulkumaran S, Egawa T, Ishikawa H, Umeno M and Jimbo T 2001 Effects of annealing on Ti, Pd, and Ni/n-Al_{0.11}Ga_{0.89}N schottky diodes *IEEE Trans. Electron Devices* **48** 573–80
- [44] Mochizuki K, Terano A, Kaneda N, Mishima T, Ishigaki T and Tsuchiya T 2011 Analysis of leakage current at Pd/AlGaIn Schottky barriers formed on GaN free-standing substrates *Appl. Phys. Express* **4** 024104
- [45] Shin J H, Park J, Jang S, Jang T and Sang Kim K 2013 Metal induced inhomogeneous schottky barrier height in AlGaIn/GaN schottky diode *Appl. Phys. Lett.* **102** 243505
- [46] Sorifi S, Moun M, Kaushik S and Singh R 2020 High-temperature performance of a GaSe nanosheet-based broadband photodetector *ACS Appl. Electron. Mater.* **2** 670–6
- [47] Mukherjee B, Cai Y, Tan H R, Feng Y P, Tok E S and Sow C H 2013 NIR schottky photodetectors based on individual single-crystalline GeSe nanosheet *ACS Appl. Mater. Interfaces* **5** 9594–604
- [48] So H and Senesky D G 2016 Rapid fabrication and packaging of AlGaIn/GaN high-temperature ultraviolet photodetectors using direct wire bonding *J. Phys. D: Appl. Phys.* **49** 285109
- [49] Tang X, Ji F, Wang H, Jin Z, Li H, Li B and Wang J 2021 Temperature enhanced responsivity and speed in an AlGaIn/GaN metal-heterostructure-metal photodetector *Appl. Phys. Lett.* **119** 013503